Enhanced mid-to-near-infrared second harmonic generation in silicon plasmonic microring resonators with low pump power

Jihua Zhang,[1,2] Eric Cassan,[2,3] and Xinliang Zhang[1,*]

[1]*Wuhan National Laboratory for Optoelectonics & School of Optical and Electronic Information, Huazhong University of Science and Technology, Wuhan 430074, China*
[2]*Institut d' Electronique Fondamentale, Université Paris-Sud, Orsay 91405, France*
[3]*e-mail: eric.cassan@u-psud.fr*
**Corresponding author: xlzhang@mail.hust.edu.cn*

Received July 11, 2014; revised August 14, 2014; accepted August 19, 2014;
posted August 21, 2014 (Doc. ID 216652); published September 24, 2014

We propose an efficient and low-power second harmonic generation (SHG) process in a silicon-compatible hybrid plasmonic microring resonator. By making the microring resonator doubly resonant at the fundamental wavelength of 3.1 μm and second harmonic wavelength of 1.55 μm, the SHG efficiency is enhanced by almost two orders of magnitude when compared to the previous result induced in a straight plasmonic waveguide. A SHG efficiency of 13.71% is predicted for a low pump power of 20 mW in a ring with radius of 2.325 μm. This device provides a potential route for realizing efficient frequency conversion between mid-infrared and near-infrared wavebands on a chip.

OCIS codes: (190.2620) Harmonic generation and mixing; (230.5750) Resonators; (250.4390) Nonlinear optics, integrated optics; (250.5403) Plasmonics.
http://dx.doi.org/10.1364/PRJ.2.000143

1. INTRODUCTION

Over the last few decades, silicon photonics has been extensively studied to operate near the telecommunication band in the near-infrared (NIR) wavelength region. Recently, mid-infrared (MIR) silicon photonics has also attracted considerable attention due to the relatively low intrinsic loss of silicon in this waveband range typically from 2 to 8 μm and to the existence of various application areas [1–6], including sensing, medical diagnostics, thermal imaging, and free-space communications [7]. It is thus interesting and significant to bridge these two wavelength bands through nonlinear wavelength conversion, such as generation of MIR light with a telecom-band pump source [8]. Another motivation for this lies in the challenges related to the detection of MIR waves. The size of detectors is usually bulky, or a cryogenic environment is often needed, which limits the development of the integration level and hinders the low-power consumption of MIR systems. A MIR-to-NIR conversion then allows circumventing these drawbacks by detecting the converted waves using mature telecom-band photodetectors [9,10].

To date, MIR-to-NIR proposed converters in silicon photonics have mostly exploited nonlinear four-wave mixing processes in silicon itself [10,11]. However, improvements in the performance of nonlinear mechanisms by introducing plasmonic structures or highly nonlinear materials such as organic polymers (NPs) into the silicon photonics platform have also been envisaged as a key option [12–19]. Plasmonic structures indeed support strong local-enhanced confinement of light in subwavelength scales and ultrafast responses [12,20], and NPs usually have nonlinear susceptibilities exceeding those of silicon or even have large second-order nonlinear susceptibilities that vanish in silicon [18,19]. Microring resonators (MRRs) have also been proposed to be attractive components in silicon photonics to further reinforce optical nonlinearities and realize efficient and compact nonlinear frequency conversions because of the large field enhancements around resonant wavelengths provided by MRRs [21–28]. The combination of hybrid plasmonic waveguides (HPWs) and MRRs has been proposed in several works in which the HPW-based MRRs support subwavelength or even submicrometer radii and large field enhancements in the low-index slot area [29–33]. However, most of these works were focused on the linear response of the MRR. In this work, we apply the HPW of Ref. [15] into a MRR configuration. By setting both the fundamental frequency (FF) and the second harmonic frequency (SHF) at two different resonant wavelengths, an enhancement factor of second harmonic generation (SHG) efficiency by almost two orders of magnitude is predicted.

The remainder of this paper is organized as follows. In Section 2, we describe the structure of the proposed HPW-MRR device and the detailed design to take the phase matching, resonance, and optical losses of the MRR into account. In Section 3, results related to SHG in the proposed configuration are presented. Finally, we conclude in Section 4.

2. STRUCTURE AND DESIGN

A. Structure

The proposed silicon-organic hybrid plasmonic microring resonator (SOHPMR) is shown in Fig. 1. The straight access waveguide with width w_a is coupled with the ring through

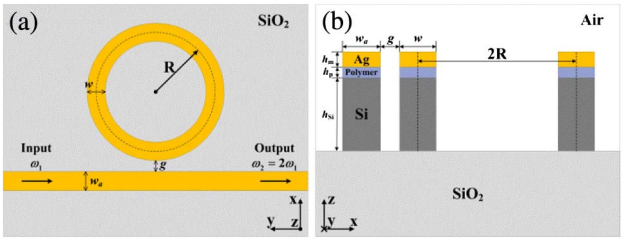

Fig. 1. Schematic of the SOHPMR. Cross-sectional views along the (a) $X-Y$ and (b) $X-Z$ planes.

a gap distance of g. The radius and width of the bended waveguide are R and w, respectively. The cross section of the HPW is characterized by a NP with a thickness of $h_p = 70$ nm, well suited to find a phase-matching point in a bended waveguide, as shown hereafter. The thicknesses of the Ag and Si layers are $h_m = 100$ nm and $h_{\mathrm{Si}} = 480$ nm, respectively. The polymer is chosen as the doped, cross-linked NP with a refractive index of $n = 1.643$ and a nonlinear susceptibility of $\chi^{(2)}_{111} = 619$ pm/V at the wavelength of 1550 nm [19]. The pump light at the FF of $\lambda_1 = 3.1$ μm is coupled into the SOHPMR with reasonable powers (values are given hereafter). The expected SHF at $\lambda_2 = \lambda_1/2 = 1.55$ μm is generated and outputs from the through port of the SOHPMR.

Such a device can be fabricated by classical technological processes. First, the polymer can be spin-coated onto the silicon layer, and then by defining a mask on the wafer and etching through, the MRR configuration can be defined. Following this, metallic layers can be deposited on top through a lift-off process.

B. Design for Phase Matching, Adjustment of the Resonance, and Loss Minimization

Using the modal phase-matching method, the needed phase-matching condition (PMC) to enhance the nonlinear SHG process can be realized between the fundamental (zeroth) mode at the FF and the second-order (first) mode at the SHF in the straight HPW [15]. Based on the same mechanism, the new phase-matching points in the bend-waveguide configuration have been searched. The modal properties of bended waveguides have been analyzed by 2D axisymmetric simulation in COMSOL. Material dispersion for modeling the refractive index of SiO_2, Si, and Ag was taken from Refs. [34,35], and [36], respectively. Figure 2 shows the difference of the effective refractive index between the interacting

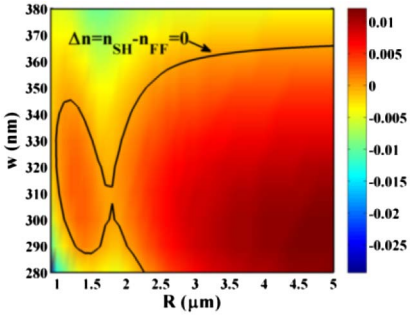

Fig. 2. $\Delta n = n_{\mathrm{SH}} - n_{\mathrm{FF}}$ as functions of the radius and width of the bended waveguides. The black line represents the zero value, i.e., the phase-matching line.

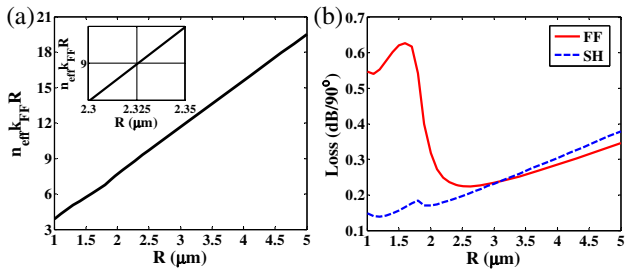

Fig. 3. (a) $n_{\mathrm{eff}}k_{\mathrm{FF}}R$ and (b) loss of a 90° bend at the phase-matching line as functions of the radius. The inset in (a) is an enlarged view near $n_{\mathrm{eff}}k_{\mathrm{FF}}R = 9$.

two modes as a function of the radius R and width w of the bended waveguide. Note that the fundamental mode of the SHF was not considered in this study. The black line marks out the zero value, i.e., the phase-matching line. One can see that the PMC can be fulfilled in the bended HPW as well and that for most of the radius values, two phase-matching points can be found.

Next, the locations of the resonant wavelengths for the ring have been adjusted in order to match with the two frequencies of interest for the reinforcement of the SHG process. Stating that a resonance into the ring happens when $n_{\mathrm{eff}}k_{\mathrm{FF}}R = m$ (m is an integer and is known as the azimuthal number of the resonance), where n_{eff} and k_{FF} are the effective refractive index and propagation constant, respectively, the "$n_{\mathrm{eff}}k_{\mathrm{FF}}R$" quantity has been plotted as a function of radius in Fig. 3(a). For each radius value, the larger waveguide width on the top phase-matching line has been chosen correspondingly. Combining this condition with the minimization of the 90°-bending HPW losses for the two frequencies of interest [shown in Fig. 3(b)], the $m = 9$ value was finally chosen. Optimal radii near 2.6 and 2 μm were found for the FF and the SHF, respectively, where a minimum loss level was obtained due to the joint contributions from the radiation (increasing exponentially with a radius decrease) and the intrinsic losses of the waveguide resulting from the metal absorption [30]. As shown in the inset of Fig. 3(a), the corresponding geometrical parameters for $m = 9$ are $R = 2.325$ μm and $w = 351$ nm ≈ 350 nm, which are the final geometrical parameters that were chosen.

The obtained phase-matched field distributions are shown in Fig. 4, where Figs. 4(a) and 4(b) plot the E_z distributions of the zeroth mode at the FF and the first mode at the SHF, respectively. The effective refractive indices of the two modes are $n_{\mathrm{FF}} = 1.90963 + 0.00362\mathrm{i}$ and $n_{\mathrm{SH}} = 1.90961 + 0.00144\mathrm{i}$, respectively. Figure 4(c) shows the normalized E_z profiles on the center line of the slot along the r direction, as marked in Fig. 4(a). We can see that the peak value of the field is not

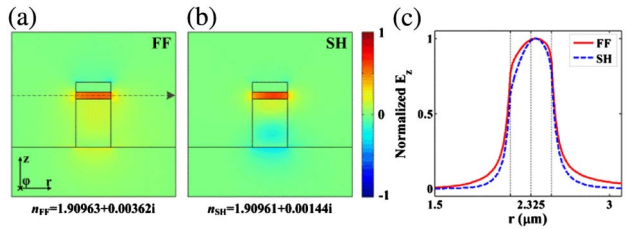

Fig. 4. E_z distributions for the phase-matched modes at (a) FF and (b) SHF when $R = 2.325$ μm and $w = 351$ nm. (c) is the normalized E_z distribution on the center line of the slot along the r direction.

located at the center of the waveguide because of the bended-waveguide property.

The width of the access waveguide was then designed as $w_a = 358.3\ \text{nm} \approx 360\ \text{nm}$ in order to maximize the fraction of FF field coupled into the ring. Then, $n_{\text{FF}} = 1.90968 + 0.00271\text{i}$ and $n_{\text{SH}} = 1.91268 + 0.00139\text{i}$ for the access waveguide. Finally, in order to set a comparison benchmark for the SHG efficiency in the ring resonator configuration with previous results, the efficiency of the SHG process in a straight HPW was complementarily estimated (with $w = 369.2\ \text{nm} \approx 370\ \text{nm}$ in this case for PMC consideration).

3. THEORY AND RESULTS

A. Second Harmonic Generation Enhancement Factor in the Ring Resonator

In this subsection, we derive the enhancement factor for the SHG in a ring resonator when compared to a single waveguide. First, the SHG efficiency in a single lossy waveguide with a length of L is (the detailed derivation is given in Appendix A)

$$\eta_1 = \frac{P_{\text{SH}}^{(\text{out})}}{P_{\text{FF}}^{(\text{in})}} = \frac{\omega_{\text{FF}}^2}{16} c_{\text{SH}}^2 L_{\text{eff}}^2(L)\ \exp(-\alpha_{\text{SH}} L) P_{\text{FF}}(0), \tag{1}$$

where $P_{\text{FF}}^{(\text{in})}$ and $P_{\text{SH}}^{(\text{out})}$ are the input power of the FF and the generated output power of the SHF, respectively. ω_{FF} is the angular frequency of the FF, c_{SH} is the nonlinear coupling coefficient being the overlap integral between the interacting modes in the nonlinear cross-sectional area, and L_{eff} is the effective length defined by

$$L_{\text{eff}}(L) = \frac{1 - \exp[-(\alpha_{\text{FF}} - \alpha_{\text{SH}}/2 + i\Delta\beta)L]}{\alpha_{\text{FF}} - \alpha_{\text{SH}}/2 + i\Delta\beta}. \tag{2}$$

$\Delta\beta = \beta_{\text{SH}} - 2\beta_{\text{FF}}$ is the phase mismatch. $\beta_{\text{FF,SH}}$ and $\alpha_{\text{FF,SH}}$ represent the phase propagation constant and attenuation coefficient, respectively.

For the SHG in a MRR, the conversion efficiency is (Appendix B)

$$\eta_2 = \frac{P_{\text{SH}}^{(\text{out})}}{P_{\text{FF}}^{(\text{in})}} = \frac{\omega_{\text{FF}}^2}{16} c_{\text{SH}}^2 L_{\text{eff}}^2(L) F_{\text{FF}}^4 F_{\text{SH}}^2\ \exp(-\alpha_{\text{SH}} L) P_{\text{FF}}^{(\text{in})}. \tag{3}$$

Here L is the circumference of the microring given by $L = 2\pi R$ with R being the radius of the ring measured from the center of the ring to the center of the waveguide. $F_{\text{FF,SH}}$ are the field enhancement factors, which can be written as

$$F_{\text{FF,SH}} = \frac{\kappa_{\text{FF,SH}}}{1 - t_{\text{FF,SH}}\ \exp[(i\beta_{\text{FF,SH}} - \alpha_{\text{FF,SH}}/2)L]}. \tag{4}$$

κ and t are the coupling and transmission coefficients related to each other by $|\kappa|^2 + |t|^2 = 1$.

Compared to the SHG efficiency in a single waveguide of Eq. (1), the efficiency in a MRR is enhanced by a factor of $F_{\text{FF}}^4 F_{\text{SH}}^2$. However, it should be noted that the linear losses of the bended waveguide in the MRR here include the intrinsic loss of the waveguide and the bend radiation loss, which makes them larger than that for a straight waveguide. The real enhancement factor would thus be smaller than $F_{\text{FF}}^4 F_{\text{SH}}^2$. Specifically, at the considered phase-matching and resonating point considered in this study, where $\beta_{\text{SH}} = 2\beta_{\text{FF}} = 2m/R$ with m being an integer, the effective length and field enhancement factor are

$$L_{\text{eff}}(L) = \frac{1 - \exp[-(\alpha_{\text{FF}} - \alpha_{\text{SH}}/2)L]}{\alpha_{\text{FF}} - \alpha_{\text{SH}}/2},$$
$$F_{\text{FF,SH}} = \frac{\kappa_{\text{FF,SH}}}{1 - t_{\text{FF,SH}}\ \exp\left(-\frac{\alpha_{\text{FF,SH}}}{2} L\right)}. \tag{5}$$

In this circumstance, SHG shows the best performance.

B. Obtained Enhanced Second Harmonic Generation Conversion Efficiencies

In the first benchmarking single straight HPW considered configuration, the nonlinear coupled coefficient was calculated to be $c_{\text{SH}} = 134\ \text{psm}^{-1}\ \text{W}^{-1/2}$. Then by using Eq. (1), the SHG efficiency was estimated as $\eta_1 = 0.14\%$ for an input pump power $P_{\text{FF}}^{(\text{in})} = 20\ \text{mW}$ and a waveguide length of 14.6 μm corresponding to the unfolded circumference of the MRR considered in a second step. Similarly, by using Eq. (3), the SHG efficiency was newly obtained in the MRR configuration under the same pumping power condition. The nonlinear coupled coefficient was then $c_{\text{SH}} = 130\ \text{psm}^{-1}\ \text{W}^{-1/2}$ for the bended-waveguide case. Figure 5 shows the final MRR-enhanced SHG efficiency η_2 as a function of the two waveguide-to-ring transmission coefficients for the FF (t_{FF}) and the SHF (t_{SH}), respectively (see Appendix B for the exact definitions of t_{FF} and t_{SH}, which are in practice controlled by the geometrical sizes of the access and bended waveguides, and the gap g between them). As is visible, a peak efficiency up to $\eta_2 = 21\%$ is realized when the MRR works at the critical coupling point for both the FF and the SHF, i.e., when $t_{\text{FF}} = \exp(-\pi\alpha_{\text{FF}} R) = 0.898$ and $t_{\text{SH}} = \exp(-\pi\alpha_{\text{SH}} R) = 0.918$. A maximum enhancement factor of $\eta_2/\eta_1 = 150$ is then expected. However, it is worth noting that it is not possible to let the FF and the SHF work at the critical coupling points at the same time in practice. Usually, t_{SH} is larger than t_{FF} for the same MRR because the waveguide mode at the SHF extends less beyond the waveguide boundary due to a smaller wavelength. In spite of this, an optimal point can be envisaged in practice by adjusting the geometrical parameters of the MRR.

All the other geometrical parameters being fixed, the coupling and transmission coefficients of the MRR are only controlled by the thickness of the gap g between the access waveguide and the ring. Figure 6(a) shows the transmission coefficients for the two wavelengths of interest as a function

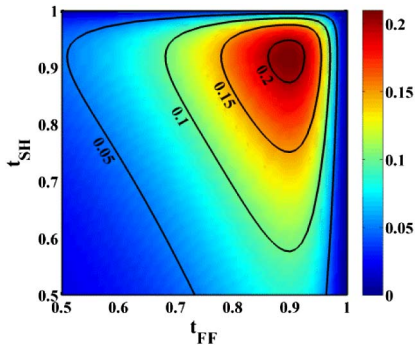

Fig. 5. SHG efficiency η_2 as a function of the transmission coefficients for FF t_{FF} and SHF t_{SH}.

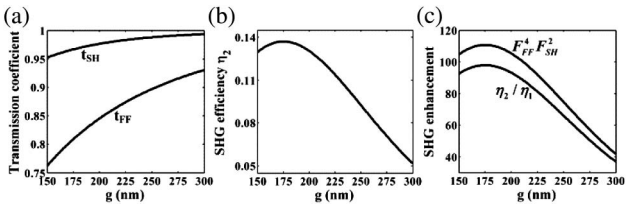

Fig. 6. (a) Transmission coefficients for two wavelengths, (b) final SHG conversion efficiency, and (c) enhancement factor in the ring as a function of the gap.

of the gap parameter g. Here the coupling coefficients are calculated by making use of the coupled mode theory for MRRs [37,38]. Figure 6(b) shows the corresponding SHG conversion efficiency for different gap thicknesses. As can be seen, there is an optimal gap of $g = 175$ nm, where the SHG efficiency is $\eta_2 = 13.71\%$. Correspondingly, $t_{FF} = 0.8088$ and $t_{SH} = 0.9666$, respectively. Figure 6(c) shows the SHG enhancement factor described by $F_{FF}^4 F_{SH}^2$ and the realistic enhancement η_2/η_1 ratio as functions of g. For the optimal gap of 175 nm, a maximum enhancement up to $\eta_2/\eta_1 \sim 100$ is thus possible in practice by changing the straight HPW configuration into the MRR one. Another interesting point lies in the critical point for the FF, where no FF light would couple out from the through port. It happens when $g = 251$ nm ≈ 250 nm. At this point, $t_{FF} = 0.898$ and $t_{SH} = 0.988$. The SHG efficiency is then $\eta_2 = 9.2\%$, which means a MRR-enhancement factor of still 66.

In order to further confirm the veracity of the proposed scheme, we calculated the transmission spectra of the MRR around the SHF and the FF in a 3D structure and plot them in Fig. 7. FDTD Lumerical software was used to carry out the 3D full-wave simulation. Two resonant wavelengths of 1548.4

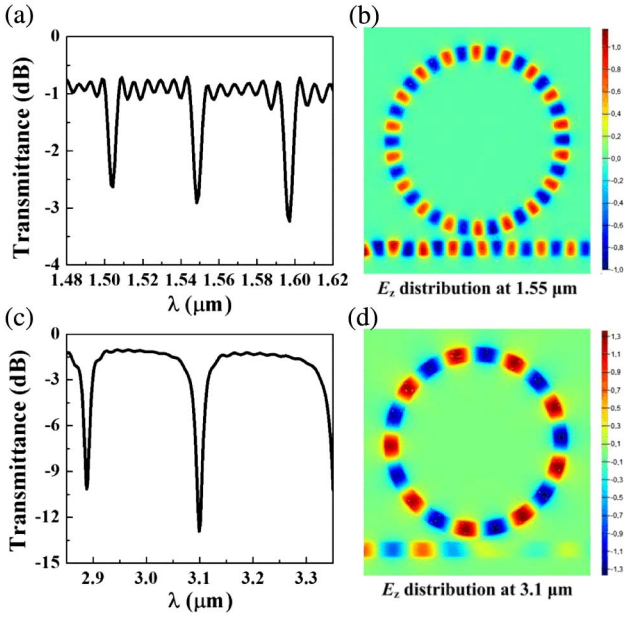

Fig. 7. Transmission spectra of the 3D MRR structure around (a) SHF of 1.55 μm and (c) FF of 3.1 μm when $R = 2.325$ μm, $w_a = 358.3$ nm, $w = 351$ nm, and $g = 175$ nm. The two resonant wavelengths are 1548.4 and 3099 nm. (b) and (d) are the E_z distributions at the SHF and the FF, respectively.

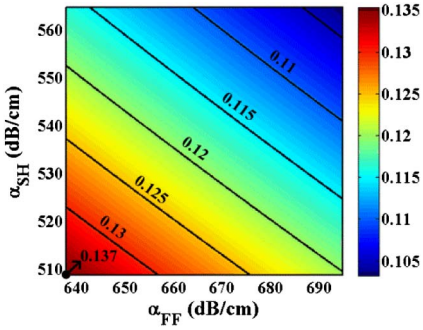

Fig. 8. SHG efficiency η_2 as a function of the attenuation coefficients for FF (α_{FF}) and SHF (α_{SH}).

and 3099 nm are presented. The slight difference over the previous mode analysis is probably due to the applied different mesh sizes and different calculation methods in the finite-element-based mode analysis and 3D full-wave FDTD simulation. The MRR shows small extinction ratios because it works deviating from the critical points especially at the SHF. Figures 7(b) and 7(d) show the E_z distributions at the SHF and the FF, respectively. As can be seen, the MRR resonates at both the FF and the SHF and the azimuthal numbers at two wavelengths are 9 and 18, respectively. This agrees well with the previous mode analysis.

In the meantime, we finally estimated the robustness of the present results with respect to the additional optical losses due to the side-wall roughness coming from lithographic and etching steps used to define the investigated structure. In this purpose, we considered the last optimized configuration with loss coefficients of the bended HPW at the FF and the SHF given by $\alpha_{FF} = 638$ dB/cm and $\alpha_{SH} = 509$ dB/cm, respectively, and anticipated from this initial condition an increase of α_{FF} and α_{SH}. The result is plotted in Fig. 8, in which the left bottom corner corresponds to the bottom loss level coming from the absorption of the metallic layer and radiation losses only. As shown here, the SHG efficiency only slightly drops from 13% to 10% even for extremely large extrinsic losses eventually coming from the fabrication process. This point and the quantitative results provided by the 3D performed FDTD simulations (Fig. 7) assess the strong potential of the proposed approach for SHG enhancement in the ultrasmall footprint silicon plasmonic ring resonator structures.

4. CONCLUSION

To conclude, a silicon-organic HPW geometry based on a microring configuration is proposed to enhance the SHG process on the silicon photonics platform. By taking the phase matching, resonance, and loss level into consideration, the conversion properties are shown to be improved in three aspects: the needed pump power becomes lower, the size of the device is smaller, and the efficiency of the SHG is larger. In the proposed final geometry, a SHG conversion efficiency of around 13.7% is predicted for a pump power as low as 20 mW and a ring radius of 2.325 μm. This obtained dramatic improvement of the nonlinear efficiency with respect to previous results opens avenues to practical applications using low-power nonlinear SHG-based all-optical on-chip signal processing.

APPENDIX A: THEORY OF SECOND HARMONIC GENERATION IN A SINGLE WAVEGUIDE

In a single lossy waveguide propagating along the $+z$ direction, the nonlinear coupled equations (NCEs) for the SHG are [14]

$$\frac{\partial A_{\mathrm{FF}}}{\partial z} = -\frac{\alpha_{\mathrm{FF}}}{2}A_{\mathrm{FF}} + i\frac{\omega_{\mathrm{FF}}}{4}c_{\mathrm{FF}}A_{\mathrm{FF}}^{*}A_{\mathrm{SH}}\ \exp(i\Delta\beta z),$$
$$\frac{\partial A_{\mathrm{SH}}}{\partial z} = -\frac{\alpha_{\mathrm{SH}}}{2}A_{\mathrm{SH}} + i\frac{\omega_{\mathrm{FF}}}{4}c_{\mathrm{SH}}A_{\mathrm{FF}}A_{\mathrm{FF}}\ \exp(-i\Delta\beta z), \tag{A.1}$$

where ω_{FF} is the angular frequency of the FF. $A_{\mathrm{FF,SH}}$ are the slowly varied complex mode amplitudes. $\Delta\beta = \beta_{\mathrm{SH}} - 2\beta_{\mathrm{FF}}$ is the phase mismatch. $\beta_{\mathrm{FF,SH}}$ and $\alpha_{\mathrm{FF,SH}}$ represent the phase propagation constant and attenuation coefficient, respectively. And $c_{\mathrm{FF,SH}}$ are the nonlinear coupling coefficients, which are defined by

$$c_{\mathrm{FF}} = \varepsilon_0 \iint \left\{\chi^{(2)} : \vec{E}_{\mathrm{SH}}(x,y)\vec{E}_{\mathrm{FF}}^{*}(x,y)\cdot\vec{E}'_{\mathrm{FF}}(x,y)\right\}\mathrm{d}x\mathrm{d}y,$$
$$c_{\mathrm{SH}} = \varepsilon_0 \iint \left\{\chi^{(2)} : \vec{E}_{\mathrm{FF}}(x,y)\vec{E}_{\mathrm{FF}}(x,y)\cdot\vec{E}'_{\mathrm{SH}}(x,y)\right\}\mathrm{d}x\mathrm{d}y, \tag{A.2}$$

with $\vec{E}_{\mathrm{FF,SH}}(x,y)$ and $\vec{E}'_{\mathrm{FF,SH}}(x,y)$ being the mode profiles, which have been normalized. $\vec{E}'_{\mathrm{FF,SH}}(x,y)$ are the modes propagating along the $-z$ direction. Under the approximation in which the pump is not depleted by the nonlinear conversion process, one can solve Eq. (A.1) analytically to obtain [39]

$$A_{\mathrm{FF}} = A_{\mathrm{FF}}(0)\ \exp\left(-\frac{\alpha_{\mathrm{FF}}}{2}z\right),$$
$$A_{\mathrm{SH}} = i\frac{\omega_{\mathrm{FF}}}{4}c_{\mathrm{SH}}L_{\mathrm{eff}}(z)A_{\mathrm{FF}}^{2}(0)\ \exp\left(-\frac{\alpha_{\mathrm{SH}}}{2}z\right),$$
$$+ A_{\mathrm{SH}}(0)\ \exp\left(-\frac{\alpha_{\mathrm{SH}}}{2}z\right), \tag{A.3}$$

where the effective length is

$$L_{\mathrm{eff}}(z) = \frac{1-\exp[-(\alpha_{\mathrm{FF}}-\alpha_{\mathrm{SH}}/2+i\Delta\beta)z]}{\alpha_{\mathrm{FF}}-\alpha_{\mathrm{SH}}/2+i\Delta\beta}. \tag{A.4}$$

So the SHG efficiency in a lossy waveguide with length of L is

$$\eta_1 = \frac{|A_{\mathrm{SH}}(L)|^2}{|A_{\mathrm{FF}}(0)|^2} = \frac{\omega_{\mathrm{FF}}^2}{16}c_{\mathrm{SH}}^2L_{\mathrm{eff}}^2(L)\ \exp(-\alpha_{\mathrm{SH}}L)P_{\mathrm{FF}}(0). \tag{A.5}$$

Note that this single waveguide can be a straight or a bended waveguide.

APPENDIX B: THEORY OF SECOND HARMONIC GENERATION IN A MICRORING RESONATOR

Next, we deduce the theory of SHG in a MRR, starting from the schematic of Fig. 9. The interactive waves satisfy the following equations:

$$A_{\mathrm{FF,SH}}^{(2)} = t_{\mathrm{FF,SH}}A_{\mathrm{FF,SH}}^{(1)} + i\kappa_{\mathrm{FF,SH}}A_{\mathrm{FF,SH}}^{(4)},$$
$$A_{\mathrm{FF,SH}}^{(3)} = i\kappa_{\mathrm{FF,SH}}A_{\mathrm{FF,SH}}^{(1)} + t_{\mathrm{FF,SH}}A_{\mathrm{FF,SH}}^{(4)}. \tag{B.1}$$

The complex mode amplitudes A are normalized, so that their squared magnitude corresponds to the modal power. κ and t are coupling and transmission coefficients with $|\kappa|^2 + |t|^2 = 1$. Besides, based on Eq. (A.3), we can obtain

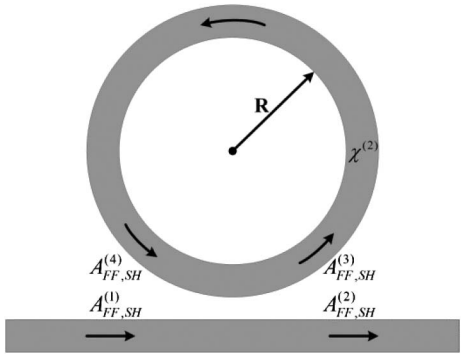

Fig. 9. Schematic of SHG in a single-pass MRR.

$$A_{\mathrm{FF}}^{(4)} = A_{\mathrm{FF}}^{(3)}\ \exp\left[\left(i\beta_{\mathrm{FF}} - \frac{\alpha_{\mathrm{FF}}}{2}\right)L\right],$$
$$A_{\mathrm{SH}}^{(4)} = i\frac{\omega_{\mathrm{FF}}}{4}c_{\mathrm{SH}}L_{\mathrm{eff}}(L)\left[A_{\mathrm{FF}}^{(3)}\right]^2\ \exp\left[\left(i\beta_{\mathrm{SH}} - \frac{\alpha_{\mathrm{SH}}}{2}\right)L\right]$$
$$+ A_{\mathrm{SH}}^{(3)}\ \exp\left[\left(i\beta_{\mathrm{SH}} - \frac{\alpha_{\mathrm{SH}}}{2}\right)L\right], \tag{B.2}$$

where L is the circumference of the microring given by $L = 2\pi R$ with R being the radius of the ring. $L_{\mathrm{eff}}(L)$ is the effective length defined in Eq. (A.4). The incident condition of the SHG is

$$A_{\mathrm{FF}}^{(1)} = A_{\mathrm{FF}}^{(\mathrm{in})}, \qquad A_{\mathrm{SH}}^{(1)} = 0. \tag{B.3}$$

Based on Eqs. (B.1)–(B.3), we can obtain

$$A_{\mathrm{FF}}^{(2)} = \left\{t_{\mathrm{FF}} - \kappa_{\mathrm{FF}}F_{\mathrm{FF}}\ \exp\left[\left(i\beta_{\mathrm{FF}} - \frac{\alpha_{\mathrm{FF}}}{2}\right)L\right]\right\}A_{\mathrm{FF}}^{(\mathrm{in})},$$
$$A_{\mathrm{FF}}^{(3)} = iF_{\mathrm{FF}}A_{\mathrm{FF}}^{(\mathrm{in})},$$
$$A_{\mathrm{FF}}^{(4)} = iF_{\mathrm{FF}}\ \exp\left[\left(i\beta_{\mathrm{FF}} - \frac{\alpha_{\mathrm{FF}}}{2}\right)L\right]A_{\mathrm{FF}}^{(\mathrm{in})},$$
$$A_{\mathrm{SH}}^{(2)} = \frac{\omega_{\mathrm{FF}}}{4}c_{\mathrm{SH}}L_{\mathrm{eff}}(L)F_{\mathrm{FF}}^2F_{\mathrm{SH}}\ \exp\left[\left(i\beta_{\mathrm{SH}} - \frac{\alpha_{\mathrm{SH}}}{2}\right)L\right]\left[A_{\mathrm{FF}}^{(\mathrm{in})}\right]^2,$$
$$A_{\mathrm{SH}}^{(3)} = -i\frac{\omega_{\mathrm{FF}}}{4}\frac{t_{\mathrm{SH}}}{\kappa_{\mathrm{SH}}}c_{\mathrm{SH}}L_{\mathrm{eff}}(L)F_{\mathrm{FF}}^2F_{\mathrm{SH}}\ \exp\left[\left(i\beta_{\mathrm{SH}} - \frac{\alpha_{\mathrm{SH}}}{2}\right)L\right]\left[A_{\mathrm{FF}}^{(\mathrm{in})}\right]^2,$$
$$A_{\mathrm{SH}}^{(4)} = -i\frac{\omega_{\mathrm{FF}}}{4\kappa_{\mathrm{SH}}}c_{\mathrm{SH}}L_{\mathrm{eff}}(L)F_{\mathrm{FF}}^2F_{\mathrm{SH}}\ \exp\left[\left(i\beta_{\mathrm{SH}} - \frac{\alpha_{\mathrm{SH}}}{2}\right)L\right]\left[A_{\mathrm{FF}}^{(\mathrm{in})}\right]^2, \tag{B.4}$$

where the $F_{\mathrm{FF,SH}}$ are the field enhancement factors, which can be written as

$$F_{\mathrm{FF,SH}} = \frac{\kappa_{\mathrm{FF,SH}}}{1 - t_{\mathrm{FF,SH}}\ \exp[(i\beta_{\mathrm{FF,SH}} - \alpha_{\mathrm{FF,SH}}/2)L]}. \tag{B.5}$$

The SHG conversion efficiency is

$$\eta_2 = \frac{|A_{\mathrm{SH}}^{(2)}|^2}{|A_{\mathrm{FF}}^{(\mathrm{in})}|^2} = \frac{\omega_{\mathrm{FF}}^2}{16}c_{\mathrm{SH}}^2L_{\mathrm{eff}}^2(L)F_{\mathrm{FF}}^4F_{\mathrm{SH}}^2\ \exp(-\alpha_{\mathrm{SH}}L)P_{\mathrm{FF}}^{(\mathrm{in})}. \tag{B.6}$$

In the analytic solution of Eqs. (A.3) and (B.2) for the NCE of Eq. (A.1), we have made an approximation that the pump is not depleted by the nonlinear conversion. Now we confirm the accuracy of this approximation by comparing the analytic solution with the numerical solution obtained by calculating the

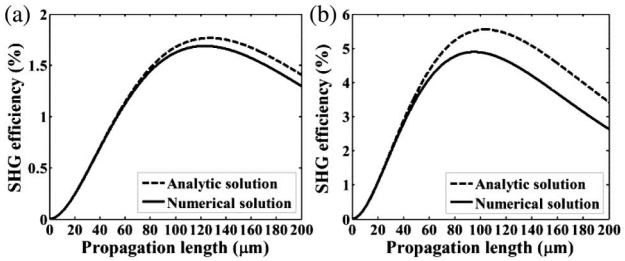

Fig. 10. Analytic solution and numerical solution of the SHG efficiency as functions of the propagation length in (a) straight waveguide and (b) bended waveguide.

NCE directly. Figure 10(a) shows the SHG efficiency as a function of the propagation length in the straight HPW when the input pump power of the FF is $P_{\mathrm{FF}}^{(\mathrm{in})} = 20$ mW. The dashed line and solid line represent the analytic solution and numerical solution, respectively. When the MRR works at the critical coupling point for the FF, i.e., $t_{\mathrm{FF}} = \exp(-\pi\alpha_{\mathrm{FF}}R)$, the field enhancement factor in Eq. (B.5) is calculated to be $F_{\mathrm{FF}} = 2.276$. The power of the FF in the MRR is $F_{\mathrm{FF}}^2 P_{\mathrm{FF}}^{(\mathrm{in})} = 103.6$ mW. Taking this power as the input power of the FF, Fig. 10(b) shows the comparison for the bend waveguide with radius of $R = 2.325$ μm. One can see that, for both the straight and bend waveguides we study in this work, the analytic solution for the NCE is accurate when the length of the waveguide is smaller than 40 μm. For the final structure we choose, the circumference of the ring is $L = 2\pi R = 14.6$ μm. Based on the above analysis, it is reasonable to apply the analytic solution in Eqs. (A.3) and (B.2). Lastly, it should be noted that this analytic solution is only applicable under the condition of low pump power and short waveguide length. Otherwise direct calculation of the NCE is required. This matter of fact explains why the conversion efficiency at large pumping powers (e.g., 200 mW, 2 W) cannot be considered by starting from 13.71% and multiplying this result by the amount of pumping power increase with respect to $P_{\mathrm{FF}} = 20$ mW.

ACKNOWLEDGMENTS

The authors acknowledge the NSFC Major International Joint Research Project (No. 61320106016), the National Basic Research Program of China (Grant No. 2011CB301704), the National Science Fund for Distinguished Young Scholars (No. 61125501), and the ANR Program Blanc International POSISLOT (2012, 9035RA13)/NSFC (612111022).

REFERENCES

1. B. Jalali and S. Fathpour, "Silicon photonics," J. Lightwave Technol. **24**, 4600–4615 (2006).
2. Z. Fang and C. Z. Zhao, "Recent progress in silicon photonics: a review," ISRN Opt. **2012**, 428690 (2012).
3. R. Soref, "Mid-infrared photonics in silicon and germanium," Nat. Photonics **4**, 495–497 (2010).
4. G. Z. Mashanovich, M. M. Milosevic, M. Nedeljkovic, N. Owens, B. Q. Xiong, E. J. Teo, and Y. F. Hu, "Low loss silicon waveguides for the mid-infrared," Opt. Express **19**, 7112–7119 (2011).
5. A. Spott, Y. Liu, T. W. Baehr-Jones, R. Ilic, and M. Hochberg, "Mid-infrared photonics in silicon," Proc. SPIE **7917**, 79171B (2011).
6. M. M. Milosevic, M. Nedeljkovic, T. M. Ben Masaud, E. Jaberansary, H. M. H. Chong, N. G. Emerson, G. T. Reed, and G. Z. Mashanovich, "Silicon waveguides and devices for the mid-infrared," Appl. Phys. Lett. **101**, 121105 (2012).
7. R. Soref, "Toward silicon-based longwave integrated optoelectronics (LIO)," Proc. SPIE **689**, 689809 (2008).
8. S. Zlatanovic, J. S. Park, S. Moro, J. M. C. Boggio, I. B. Divliansky, N. Alic, S. Mookherjea, and S. Radic, "Mid-infrared wavelength conversion in silicon waveguides using ultracompact telecom-band-derived pump source," Nat. Photonics **4**, 561–564 (2010).
9. E. K. Tien, Y. W. Huang, S. M. Gao, Q. Song, F. Qian, S. K. Kalyoncu, and O. Boyraz, "Discrete parametric band conversion in silicon for mid-infrared applications," Opt. Express **18**, 21981–21989 (2010).
10. X. P. Liu, B. Kuyken, G. Roelkens, R. Baets, R. M. Osgood, and W. M. J. Green, "Bridging the mid-infrared-to-telecom gap with silicon nanophotonic spectral translation," Nat. Photonics **6**, 667–671 (2012).
11. B. Kuyken, X. Liu, R. Osgood, Y. Vlasov, G. Roelkens, R. Baets, and W. M. Green, "Frequency conversion of mid-infrared optical signals into the telecom band using nonlinear silicon nanophotonic wires," in *Optical Fiber Communication Conference/National Fiber Optic Engineers Conference 2011*, OSA Technical Digest (CD) (Optical Society of America, 2011), paper OThU4.
12. M. Kauranen and A. V. Zayats, "Nonlinear plasmonics," Nat. Photonics **6**, 737–748 (2012).
13. L. Alloatti, D. Korn, C. Weimann, C. Koos, W. Freude, and J. Leuthold, "Second-order nonlinear silicon-organic hybrid waveguides," Opt. Express **20**, 20506–20515 (2012).
14. J. Zhang, E. Cassan, D. Gao, and X. Zhang, "Highly efficient phase-matched second harmonic generation using an asymmetric plasmonic slot waveguide configuration in hybrid polymer-silicon photonics," Opt. Express **21**, 14876–14887 (2013).
15. J. Zhang, E. Cassan, and X. Zhang, "Efficient second harmonic generation from mid-infrared to near-infrared regions in silicon-organic hybrid plasmonic waveguides with small fabrication-error sensitivity and a large bandwidth," Opt. Lett. **38**, 2089–2091 (2013).
16. J. Zhang, P. Zhao, E. Cassan, and X. Zhang, "Phase regeneration of phase-shift keying signals in highly nonlinear hybrid plasmonic waveguides," Opt. Lett. **38**, 848–850 (2013).
17. J. Zhang, E. Cassan, and X. Zhang, "Electrically controlled second-harmonic generation in silicon-compatible plasmonic slot waveguides: a new modulation scheme," Opt. Lett. **39**, 4001–4004 (2014).
18. T. W. Baehr-Jones and M. J. Hochberg, "Polymer silicon hybrid systems: a platform for practical nonlinear optics," J. Phys. Chem. C **112**, 8085–8090 (2008).
19. J. Leuthold, W. Freude, J. M. Brosi, R. Baets, P. Dumon, I. Biaggio, M. L. Scimeca, F. Diederich, B. Frank, and C. Koos, "Silicon organic hybrid technology—a platform for practical nonlinear optics," Proc. IEEE **97**, 1304–1316 (2009).
20. M. I. Stockman, "Nanoplasmonics: past, present, and glimpse into future," Opt. Express **19**, 22029–22106 (2011).
21. J. S. Levy, M. A. Foster, A. L. Gaeta, and M. Lipson, "Harmonic generation in silicon nitride ring resonators," Opt. Express **19**, 11415–11421 (2011).
22. C. Xiong, W. Pernice, K. K. Ryu, C. Schuck, K. Y. Fong, T. Palacios, and H. X. Tang, "Integrated GaN photonic circuits on silicon (100) for second harmonic generation," Opt. Express **19**, 10462–10470 (2011).
23. W. H. P. Pernice, C. Xiong, C. Schuck, and H. X. Tang, "Second harmonic generation in phase matched aluminum nitride waveguides and micro-ring resonators," Appl. Phys. Lett. **100**, 223501 (2012).
24. Z. A. F. Bi, A. Rodriguez, H. Hashemi, D. Duchesne, M. Loncar, K. M. Wang, and S. G. Johnson, "High-efficiency second-harmonic generation in doubly-resonant chi((2)) microring resonators," Opt. Express **20**, 7526–7543 (2012).
25. A. C. Turner, M. A. Foster, A. L. Gaeta, and M. Lipson, "Ultra-low power parametric frequency conversion in a silicon microring resonator," Opt. Express **16**, 4881–4887 (2008).
26. M. Ferrera, D. Duchesne, L. Razzari, M. Peccianti, R. Morandotti, P. Cheben, S. Janz, D. X. Xu, B. E. Little, S. Chu, and D. J. Moss, "Low power four wave mixing in an integrated, micro-ring resonator with Q = 1.2 million," Opt. Express **17**, 14098–14103 (2009).

27. A. Pasquazi, R. Ahmad, M. Rochette, M. Lamont, B. E. Little, S. T. Chu, R. Morandotti, and D. J. Moss, "All-optical wavelength conversion in an integrated ring resonator," Opt. Express **18**, 3858–3863 (2010).
28. Z. Q. Li, S. M. Gao, Q. A. Liu, and S. L. He, "Modified model for four-wave mixing-based wavelength conversion in silicon micro-ring resonators," Opt. Commun. **284**, 2215–2221 (2011).
29. X. Y. Zhang, A. Hu, J. Z. Wen, T. Zhang, X. J. Xue, Y. Zhou, and W. W. Duley, "Numerical analysis of deep sub-wavelength integrated plasmonic devices based on semiconductor-insulator-metal strip waveguides," Opt. Express **18**, 18945–18959 (2010).
30. D. X. Dai, Y. C. Shi, S. L. He, L. Wosinski, and L. Thylen, "Silicon hybrid plasmonic submicron-donut resonator with pure dielectric access waveguides," Opt. Express **19**, 23671–23682 (2011).
31. H. S. Chu, Y. Akimov, P. Bai, and E. P. Li, "Submicrometer radius and highly confined plasmonic ring resonator filters based on hybrid metal-oxide-semiconductor waveguide," Opt. Lett. **37**, 4564–4566 (2012).
32. S. Y. Zhu, G. Q. Lo, and D. L. Kwong, "Performance of ultracompact copper-capped silicon hybrid plasmonic waveguide-ring resonators at telecom wavelengths," Opt. Express **20**, 15232–15246 (2012).
33. F. Lou, D. Dai, L. Thylen, and L. Wosinski, "Design and analysis of ultra-compact EO polymer modulators based on hybrid plasmonic microring resonators," Opt. Express **21**, 20041–20051 (2013).
34. R. Kitamura, L. Pilon, and M. Jonasz, "Optical constants of silica glass from extreme ultraviolet to far infrared at near room temperature," Appl. Opt. **46**, 8118–8133 (2007).
35. M. J. Weber, *Handbook of Optical Materials* (CRC, 2003).
36. P. B. Johnson and R. W. Christy, "Optical constants of the noble metals," Phys. Rev. B **6**, 4370–4379 (1972).
37. K. Okamoto, *Fundamentals of Optical Waveguides* (Academic, 2010).
38. Y. Liu, T. Chang, and A. E. Craig, "Coupled mode theory for modeling microring resonators," Opt. Eng. **44**, 084601 (2005).
39. Z. Ruan, G. Veronis, K. L. Vodopyanov, M. M. Fejer, and S. Fan, "Enhancement of optics-to-THz conversion efficiency by metallic slot waveguides," Opt. Express **17**, 13502–13515 (2009).